

Modelling blood flow in coronary arteries: Newtonian or shear-thinning non-Newtonian rheology?

Original

Modelling blood flow in coronary arteries: Newtonian or shear-thinning non-Newtonian rheology? / De Nisco, Giuseppe; Lodi Rizzini, Maurizio; Verardi, Roberto; Chiastra, Claudio; Candreva, Alessandro; De Ferrari, Gaetano; D'Ascenzo, Fabrizio; Gallo, Diego; Morbiducci, Umberto. - In: COMPUTER METHODS AND PROGRAMS IN BIOMEDICINE. - ISSN 0169-2607. - ELETTRONICO. - 242:(2023). [10.1016/j.cmpb.2023.107823]

Availability:

This version is available at: 11583/2984940 since: 2024-01-09T17:57:27Z

Publisher:

ELSEVIER IRELAND LTD

Published

DOI:10.1016/j.cmpb.2023.107823

Terms of use:

This article is made available under terms and conditions as specified in the corresponding bibliographic description in the repository

Publisher copyright

Common Ground Research Network postprint versione editoriale/Version of Record, con licenza CC by nc

(Article begins on next page)



Modelling blood flow in coronary arteries: Newtonian or shear-thinning non-Newtonian rheology?

Giuseppe De Nisco^a, Maurizio Lodi Rizzini^a, Roberto Verardi^b, Claudio Chiastra^a,
Alessandro Candreva^a, Gaetano De Ferrari^b, Fabrizio D'Ascenzo^b, Diego Gallo^{a,*},
Umberto Morbiducci^a

^a Polito^{BIO} Med Lab, Department of Mechanical and Aerospace Engineering, Politecnico di Torino, Turin, Italy

^b Hemodynamic Laboratory, Department of Medical Sciences, University of Turin, Turin, Italy

ARTICLE INFO

Keywords:

Computational hemodynamics
Blood rheological properties
Wall shear stress
Helical flow
Uncertainty in cardiovascular models

ABSTRACT

Background: The combination of medical imaging and computational hemodynamics is a promising technology to diagnose/prognose coronary artery disease (CAD). However, the clinical translation of *in silico* hemodynamic models is still hampered by assumptions/idealizations that must be introduced in model-based strategies and that necessarily imply uncertainty. This study aims to provide a definite answer to the open question of how to properly model blood rheological properties in computational fluid dynamics (CFD) simulations of coronary hemodynamics.

Methods: The geometry of the right coronary artery (RCA) of 144 hemodynamically stable patients with different stenosis degree were reconstructed from angiography. On them, unsteady-state CFD simulations were carried out. On each reconstructed RCA two different simulation strategies were applied to account for blood rheological properties, implementing (i) a Newtonian (N) and (ii) a shear-thinning non-Newtonian (non-N) rheological model. Their impact was evaluated in terms of wall shear stress (WSS magnitude, multidirectionality, topological skeleton) and helical flow (strength, topology) profiles. Additionally, luminal surface areas (SAs) exposed to shear disturbances were identified and the co-localization of paired N and non-N SAs was quantified in terms of similarity index (SI).

Results: The comparison between paired N vs. shear-thinning non-N simulations revealed remarkably similar profiles of WSS-based and helicity-based quantities, independent of the adopted blood rheology model and of the degree of stenosis of the vessel. Statistically, for each paired N and non-N hemodynamic quantity emerged negligible bias from Bland-Altman plots, and strong positive linear correlation ($r > 0.94$ for almost all the WSS-based quantities, $r > 0.99$ for helicity-based quantities). Moreover, a remarkable co-localization of N vs. non-N luminal SAs exposed to disturbed shear clearly emerged (SI distribution 0.95 [0.93, 0.97]). Helical flow topology resulted to be unaffected by blood rheological properties.

Conclusions: This study, performed on 288 angio-based CFD simulations on 144 RCA models presenting with different degrees of stenosis, suggests that the assumptions on blood rheology have negligible impact both on WSS and helical flow profiles associated with CAD, thus definitively answering to the question “is Newtonian assumption for blood rheology adequate in coronary hemodynamics simulations?”.

1. Introduction

Coronary artery disease (CAD) is the leading cause of morbidity and mortality in higher income countries and among the most investigated fields in cardiovascular medicine, with a remarkable impact on health

systems cost worldwide [1]. CAD consists in an inflammatory status caused by a complex interplay of systemic, biological, and biomechanical factors promoting lipid deposition at the arterial wall and leading to atherosclerotic plaque growth, which may result in clinical adverse events. In the context of coronary atherosclerosis, local flow

* Corresponding author. Diego Gallo, Department of Mechanical and Aerospace Engineering, Politecnico di Torino, Corso Duca degli Abruzzi, 24, 10129 Turin, Italy. Tel.: +39 011 0906574; Fax: +39 011 5646999

E-mail address: diego.gallo@polito.it (D. Gallo).

<https://doi.org/10.1016/j.cmpb.2023.107823>

Received 4 August 2023; Received in revised form 14 September 2023; Accepted 18 September 2023

Available online 19 September 2023

0169-2607/© 2023 The Author(s). Published by Elsevier B.V. This is an open access article under the CC BY license (<http://creativecommons.org/licenses/by/4.0/>).

disturbances have been associated with plaque initiation and progression and have been advocated as drivers of clinical events across the spectrum of CAD manifestations [2–4].

In the last decades, the coupling of computational fluid dynamics (CFD) and medical imaging has allowed to profile with high spatio-temporal resolution local hemodynamics in coronary arteries [5,6]. Personalized CFD models have been extensively applied to investigate the action exerted by friction forces, namely the wall shear stress (WSS), at the blood-endothelium interface, with findings supporting the so-called ‘hemodynamic risk hypothesis’ [7] of coronary atherosclerosis, which links specific WSS profiles to coronary plaques initiation, progression, and rupture. In detail, WSS profiles characterized by low cycle-average magnitude values have been associated with, e.g., local endothelial dysfunction and plaque progression [8–10], while WSS profiles characterized by high cycle-average magnitude values have been linked to plaque vulnerability [11]. More recently, a role in coronary pathophysiological processes has also emerged for (i) the variability in the contraction/expansion action exerted by the WSS on the endothelium along the cardiac cycle [3,12], and (ii) the intravascular helical flow establishing in healthy coronary vessels, which has been suggested to be atheroprotective [13,14].

The emerged evidence supporting the hemodynamic risk hypothesis for coronary arteries has highlighted the potential of personalized *in silico* modelling to lead a technological paradigm shift in CAD management, proposing itself as a non-invasive tool for a deeper understanding of the pathophysiology of the atherosclerotic process, supporting clinical decision, and predicting patient outcome by means of advanced patient-specific simulations.

However, the clinical translation of computational hemodynamics is hampered by still insufficient evidence in demonstrating the full reliability of simulated results and predictions [15,16]. The deep reason for this lies in the unavoidable assumptions/idealizations, which become sources of uncertainty that may entail the generality of the *in silico*-derived results.

In this regard, a source of uncertainty is represented by the assumptions done to model the rheological properties of blood. It is consolidated knowledge that blood has a non-Newtonian behavior with thixotropic, viscoelastic, and shear-thinning characteristics [17]. Thixotropy is associated to time scales longer than the period of the pulsatile flow cycle [17] and thus deemed to have a limited impact on coronary hemodynamics. The viscoelastic behavior at physiological hematocrit values is dominated by the viscous contribution with respect to the elastic one [18]. Therefore, the purely viscous behavior of blood as a shear-thinning fluid (i.e., the dynamic viscosity decreases with at increasing shear rates up to a value where dynamic viscosity becomes shear rate independent) [19,20] has to be considered the dominant non-Newtonian effect. However, the real need for adopting a shear-thinning non-Newtonian constitutive equation to model blood rheology in coronary *in silico* models is still debated. A paucity of studies has focused on blood rheology effects in coronary CFD, comparing the implementation of Newtonian vs. shear-thinning non-Newtonian modeling strategies (in general in terms of WSS profiles), often generalizing findings obtained on small-sized dataset ($N < 20$) [21–23] or in other arterial segments [24].

In this still unclear picture, the overarching hypothesis of this study is that shear-thinning non-Newtonian blood rheological properties might impact the coronary hemodynamics in such a way that might not be accounted for assuming Newtonian rheological properties in coronary CFD simulations. The formulated hypothesis is here tested on a dataset of patient-specific angiography-based CFD models of 144 right coronary arteries presenting different degrees of stenosis. Technically, two unsteady-state simulations were carried out on each reconstructed anatomy, assuming for blood Newtonian and shear-thinning non-Newtonian rheological properties, respectively. The influence that modeling assumptions on blood rheology have on right coronary hemodynamics is analyzed in terms of near-wall and intravascular hemodynamic

quantities with a suggested link to coronary biological adverse events.

2. Materials and Methods

2.1. Patients’ enrollment, data collection and 3D vessel reconstruction

The study enrolled 224 hemodynamically stable patients with coronary artery disease from 11 international centers. Right coronary arteries (RCAs) were considered for the study. The characteristics of the patients are summarized in Table 1.

The study was approved by each local medical hospital and conducted in accordance with the World Medical Association Declaration of Helsinki (64th WMA General Assembly, Fortaleza Brazil, October 2013) and Medical Research involving the human subject act (WMO). All patients gave their written informed consent.

A schematic overview of the study design is provided in Fig. 1. Patients underwent invasive coronary cineangiography. All angiograms were acquired and reviewed at a core laboratory. Patients presenting with an acute coronary syndrome with the RCA as culprit vessel were excluded. Additionally, an initial screening of the angiographic images allowed the exclusion of cases with overlapping or foreshortening of the segment of interest. After exclusion criteria, 144 RCA vessels were considered and their 3D geometries were reconstructed from two cranial, end-diastolic angiographic projections, with a minimum angle of 25° between them, using the clinical software QAngio XA Bifurcation RE (Medis medical imaging systems, Leiden, The Netherlands). Based on the importance of side branches for the characterization of coronary hemodynamics [25–27], each side branch with a diameter larger than 1 mm was reconstructed and merged to form the complete RCA geometry using VTK (Kitware, Inc., Clifton Park, NY, USA) and VMTK (Orobix, Bergamo, Italy) libraries, as detailed elsewhere [28]. Briefly, the main vessel was segmented and reconstructed considering one side branch at a time. Then, the Voronoi diagrams of the single branching vessels were merged into one single diagram from which the complete 3D geometry including all side branches [28] was obtained.

Table 1
Patients’ clinical characteristics

<i>N</i> = 144 subjects	
Age (years)	70 (54–86)
Sex	
Men	108 (75.0%)
Female	36 (25.0%)
Diabetes mellitus	45/141 (31.9%)
Hypertension	107/140 (76.4%)
Dyslipidemia	92/141 (65.2%)
Smoker	
Current	37/141 (26.2%)
Former	48/141 (34.0%)
No	56/141 (39.7%)
Previous MI	1/137 (0.7%)
Previous PCI	78/143 (54.5%)
Previous CABG	3/142 (2.1%)
EF (%)	60.0 (54.7–62.3)
STEMI	11/138 (8.0%)
non-STEMI	13/138 (9.4%)
Unstable Angina	27/138 (19.6%)
AS (%)	56.1 (37.2–75.1)
class C1	46 (31.9%)
AS (%)	39.0 (27.8–50.2)
class C2	77 (53.5%)
AS (%)	58.2 (48.2–68.2)
class C3	21 (14.6%)
AS (%)	74.1 (68.1–80.1)

Data are n (%), n/N_{av} (%), or median (IQR). n: number of patients in the category; N_{av} : number of patients for whom the clinical information is available; MI: myocardial infarction; PCI: percutaneous coronary intervention; CABG: coronary artery bypass graft; EF: ejection fraction; STEMI: ST-segment elevation myocardial infarction; AS: area stenosis.

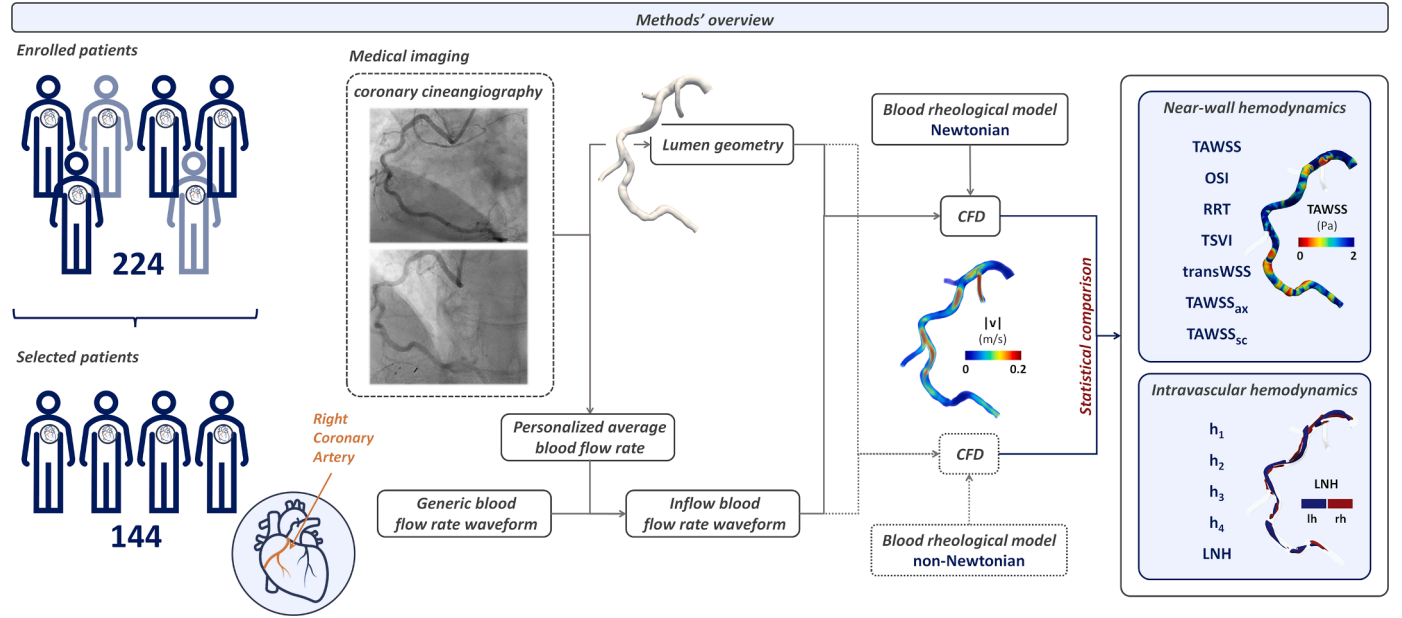


Fig. 1. Schematic diagram of the study design. Based on exclusion criteria, 80 patients of the 224 enrolled were excluded from the study. For each patient, coronary angiography was used to reconstruct the 3D geometry of the right coronary artery and to assess the contrast velocity-based average flow rate value. Newtonian and non-Newtonian models of blood rheology were adopted in CFD simulations to obtain near-wall and intravascular hemodynamic quantities. v : velocity; TAWSS: time-averaged wall shear stress; OSI: oscillatory shear index; RRT: relative residence time; TSVI: topological shear variation index; transWSS: transverse wall shear stress; ax: axial; sc: secondary; h_i ($i=1-4$): helicity-based quantities; LNH: local normalized helicity.

2.2. Computational hemodynamics

The finite volume method was applied to solve the governing equations of fluid motion in their discretized form under unsteady-state conditions using the general purpose CFD software Fluent (Ansys Inc., Canonsburg, PA, USA). The software ICEM CFD (Ansys Inc., Canonsburg, PA, USA) was used to discretize the fluid domain by using tetrahedral elements with curvature-based refinement and 5 near-wall prismatic layers. The meshing parameters were derived from a previous grid independence analysis [13,14], resulting in a mesh cardinality of 3.15 million elements on average. Blood was assumed as a homogeneous, incompressible fluid, with a density ρ equal to 1060 kg/m³. For each 3D coronary geometry two simulation strategies were adopted to model the rheological properties of blood: (i) assumption of Newtonian (N) behavior, prescribing a constant, shear rate independent blood dynamic viscosity μ equal to 0.0035 Pa·s, corresponding to a hematocrit value of 0.43, representative of the physiological hematocrit range variation (0.35–0.51) [29]; (ii) assumption of shear-thinning non-Newtonian (non-N) behavior, simulated by adopting the Carreau model, largely used in computational models of coronary hemodynamics [30,6]. The non-N Carreau model describes the relationship between viscosity and shear rate ($\dot{\gamma}$) as follows:

$$\mu = \mu_{\infty} + (\mu_0 - \mu_{\infty}) \left(1 + (\lambda \dot{\gamma})^2 \right)^{\frac{n-1}{2}} \quad (1)$$

where the nominal high shear rate viscosity μ_{∞} was set equal to the Newtonian one (0.0035 Pa·s), $\mu_0 = 0.25$ Pa·s, $\lambda = 25$ s, and $n = 0.25$ [29]. The shear rate is defined as follows:

$$\dot{\gamma} = \sqrt{2\mathbf{D}(\mathbf{v}) : \mathbf{D}(\mathbf{v})} = \sqrt{2tr(\mathbf{D}(\mathbf{v})^2)} \quad (2)$$

$$\mathbf{D}(\mathbf{v}) = \frac{\nabla \mathbf{v} + \nabla \mathbf{v}^T}{2}$$

where \mathbf{v} is the velocity vector, $\mathbf{D}(\mathbf{v})$ is the rate of deformation tensor, and $(:)$ indicates the double dot product.

Overall, 288 unsteady-state CFD simulations were performed. The

coronary vessel walls were assumed rigid, the no-slip condition was prescribed on the walls. Concerning the boundary condition definition, the 3D contrast velocity method was applied to determine the patient-specific average flow rate [11,31]. Technically, the method consists in counting the angiographic frames required for contrast to travel from the vessel ostium to a standardized distal coronary landmark, as detailed elsewhere [11]. The cycle-average flow rate (Q_{in}) can be estimated using the number of frames (N_{frames}) and the 3D distance (L) of the coronary landmark from the ostium as follows:

$$Q_{in} = A \cdot \frac{L \cdot f}{N_{frames}} \quad (3)$$

where A is the area of the inlet surface and f is frame rate of acquisition of the angiographic images.

A generalized time-dependence of flow rate waveform from Doppler-based velocity measurements in RCAs [31] was prescribed, by scaling it with respect to the estimated patient-specific value of Q_{in} . A schematization of inflow blood flow rate definition is provided in Figure S1 of the Supplementary Material. The resulting inlet flow rates were applied in terms of parabolic velocity profile, as suggested in previous studies [28]. A mean physiological heart rate of 60 bpm was considered. A diameter-based scaling law was applied to estimate the patient-specific flow split at each side branch [32], and the latter was imposed as outflow boundary condition.

A second-order accuracy scheme was applied to solve both the momentum and pressure equations with the COUPLED pressure-velocity coupling scheme. The backward Euler scheme was adopted for time integration, with a fixed time increment (the cardiac cycle was discretized in 100 time-steps). Convergence was achieved when continuity and momentum residuals fell below 10^{-5} [13,14].

2.3. Near-wall and intravascular hemodynamics

The impact of the two adopted models of blood rheology on CFD simulations was evaluated in terms of near-wall and intravascular hemodynamics. The hemodynamic quantities herein considered for the analysis are summarized in Table 2.

Table 2

Definition of hemodynamic quantities involved in the analysis.

Near-wall hemodynamic quantities	
Time-Averaged Wall Shear Stress (TAWSS)	$\text{TAWSS} = \frac{1}{T} \int_0^T \mathbf{WSS} dt$
Oscillatory Shear Index (OSI)	$\text{OSI} = 0.5 \left[1 - \frac{\left \int_0^T \mathbf{WSS} dt \right }{\int_0^T \mathbf{WSS} dt} \right]$
Relative Residence Time (RRT)	$\text{RRT} = \frac{1}{\text{TAWSS} \cdot (1 - 2\text{OSI})} = \frac{1}{\frac{1}{T} \left \int_0^T \mathbf{WSS} dt \right }$
Topological Shear Variation Index (TSVI)	$\text{TSVI} = \left\{ \frac{1}{T} \int_0^T \text{DIV}_{\mathbf{WSS}} - \overline{\text{DIV}_{\mathbf{WSS}}} ^2 dt \right\}^{1/2}$
Transverse Wall Shear Stress (transWSS)	$\text{transWSS} = \frac{1}{T} \int_0^T \left \mathbf{WSS} \cdot \left(\mathbf{n} \times \frac{\int_0^T \mathbf{WSS} dt}{\left \int_0^T \mathbf{WSS} dt \right } \right) \right dt$
Axial Wall Shear Stress (WSS _{ax})	$\text{WSS}_{\text{ax}} = \frac{\mathbf{WSS} \cdot \mathbf{C}'}{ \mathbf{C}' } \cdot \frac{\mathbf{C}'}{ \mathbf{C}' }$
Secondary Wall Shear Stress (WSS _{sc})	$\text{WSS}_{\text{sc}} = \frac{\mathbf{WSS} \cdot \mathbf{S}}{ \mathbf{S} } \cdot \frac{\mathbf{S}}{ \mathbf{S} }; \quad \mathbf{S} = \frac{\mathbf{C}' \times \mathbf{R}}{ \mathbf{C}' \mathbf{R} }$
Time-Averaged WSS _{ax} (TAWSS _{ax})	$\text{TAWSS}_{\text{ax}} = \frac{1}{T} \int_0^T \text{WSS}_{\text{ax}} dt$
Time-Averaged WSS _{sc} (TAWSS _{sc})	$\text{TAWSS}_{\text{sc}} = \frac{1}{T} \int_0^T \text{WSS}_{\text{sc}} dt$
Intravascular hemodynamic quantities	
Average Helicity (h ₁)	$h_1 = \frac{1}{T} \frac{1}{V} \int_0^T \int_V \mathbf{v} \cdot \boldsymbol{\omega} dV dt$
Average Helicity Intensity (h ₂)	$h_2 = \frac{1}{T} \frac{1}{V} \int_0^T \int_V \mathbf{v} \cdot \boldsymbol{\omega} dV dt$
Signed balance of counter-rotating helical flow structures (h ₃)	$h_3 = \frac{h_1}{h_2} - 1 \leq h_3 \leq 1$
Unsigned balance of counter-rotating helical flow structures (h ₄)	$h_4 = \frac{ h_1 }{h_2} \quad 0 \leq h_4 \leq 1$
Local Normalized Helicity (LNH)	$\text{LNH} = \frac{\mathbf{v} \cdot \boldsymbol{\omega}}{ \mathbf{v} \cdot \boldsymbol{\omega} }$

WSS is the WSS vector; **T** is the period of the cardiac cycle; **DIV_{WSS}** is the divergence of the normalized **WSS** vector; **n** is the unit vector normal to the arterial surface at each element; **C'** is the vector tangent to the centerline; **R** is the vector perpendicular to **C'** directed from the centerline to the generic point at the arterial surface, lying of the same vessel's cross-section; **S** is the vector orthogonal to vectors **R** and **C'**; **v** is the velocity vector; **ω** is the vorticity vector; **V** is the arterial volume.

Based on the widely accepted role of WSS as biomechanical factor influencing coronary vascular pathogenesis [2,10,33], several WSS-based quantities proposed in the literature were considered. In detail, the impact of the assumptions done on blood rheological properties was evaluated in terms of the three canonical WSS-based quantities, namely time-average wall shear stress magnitude (TAWSS), oscillatory shear index (OSI) [34], and relative residence time (RRT) [35]. WSS multidirectionality was quantified also in terms of transverse WSS (transWSS) [36], defined as the cycle-average WSS component acting orthogonal to the cycle-average WSS vector direction. A vessel centerline-based decomposition of the WSS was also considered, as proposed elsewhere [13]. In detail, the WSS vector projections locally aligned with the centerline of the vessel (the so-called axial WSS, WSS_{ax}) and orthogonal to it (the so-called secondary WSS, WSS_{sc}) were computed. Their magnitude was averaged along the cardiac cycle and expressed as TAWSS_{ax} and TAWSS_{sc}, respectively.

To complete the analysis, based on the recently emerged role of WSS

topological skeleton features on coronary pathophysiology [3,12], the variability in the contraction/expansion action exerted by the WSS on the endothelium along the cardiac cycle **T** was quantified in terms of the topological shear variation index (TSVI) [2,12].

Luminal surface areas (SAs) exposed to disturbed hemodynamics (low shear area: LSA, high shear area: HSA, oscillatory shear area: OSA, residence time area: RTA, transverse shear area: transSA, low axial shear area: LaxSA, high axial shear area: HaxSA, high secondary shear area: HscSA), and to high variation in WSS contraction/expansion action along the cardiac cycle (topological shear variation area: TSVA) were identified, based on objective thresholds on the patient-specific luminal distributions: both the 20th and 80th percentiles of TAWSS and TAWSS_{ax}; the 80th percentile of OSI, RRT, transWSS, TAWSS_{sc}, and TSVI. The threshold values were obtained from non-Newtonian simulations data, here considered as reference.

Intravascular hemodynamics was characterized in terms of strength, and relative rotational direction of helical blood flow structures adopting the well consolidated helicity-based quantities [37] summarized in Table 1. In detail, the net amount and the intensity of helical flow were quantified in terms of cycle-average helicity (h₁) and helicity intensity (h₂), respectively [37]. Additionally, signed (h₃) and unsigned helical rotation balance (h₄) were calculated as measure of the prevalence (identified by the sign of h₃) or only the strength (h₄) of relative rotations of helical flow structures [37].

The quantitative analysis of intravascular hemodynamics was substantiated by visualization of intravascular flow structures by means of local normalized helicity (LNH) [37], expressed as the normalized internal product between local velocity and vorticity vectors (Table 1): as a signed quantity, the visualization of LNH isosurfaces can be used to discriminate left- and right-handed helical blood flow structures [13,14,28].

The impact of the assumptions done in modelling blood rheological properties in computational models of coronary hemodynamics was investigated at the atherosclerotic lesion level of each model, expected to be mostly affected by such assumption. As detailed elsewhere [3], adopting 3D quantitative coronary angiography (QCA) the lesion segment was unambiguously defined as the coronary segment including the minimum lumen area (MLA) section of the vessel and delimited proximally and distally by the intersection of the measured lumen area curve with its linear regression, identifying the reference interpolated lumen area curve (Fig. 2).

2.4. Statistical analysis

The agreement between N and non-N simulation strategies was evaluated in terms of Bland-Altman plots [38] applied at the lesion level to paired hemodynamic quantities, taking non-N simulations as reference. This allowed to evaluate if the two simulation strategies are equivalent, in terms of the investigated hemodynamic quantities. Additionally, the Pearson correlation coefficients (*r*) were used to test the existence of linear relationships between N and non-N paired hemodynamic quantities. Significance was assumed for *p* < 0.05. The statistical analysis was performed within the Matlab environment (The MathWorks Inc., USA).

Finally, the co-localization between N and non-N SAs at the vessel level was quantitatively assessed by the similarity index (SI) [39]. The SI ranges between 0 (the SAs given by the two simulations have no spatial overlap) and 1 (the SAs are equivalent and perfectly spatially overlapped).

3. Results

The analysis was performed grouping the RCA vessels into three classes, based on the percentage area stenosis (%AS) value as measured by QCA (Table 1): class C1, %AS < 50%; class C2, 50% ≤ %AS ≤ 70%; class C3, %AS > 70%.

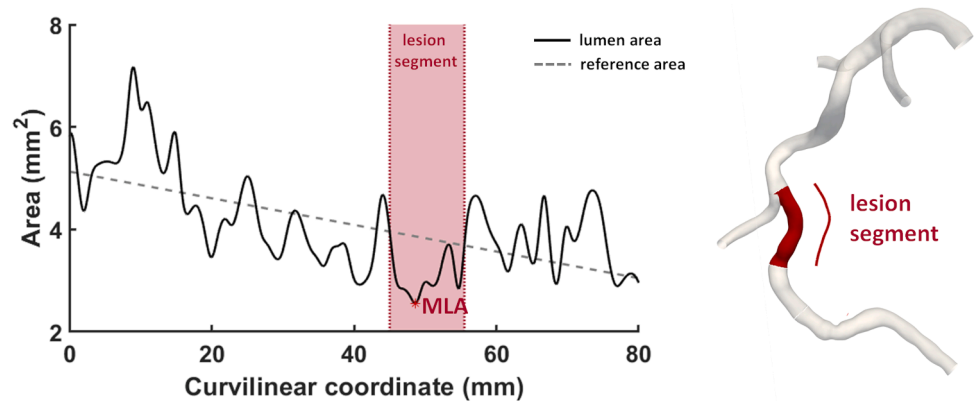


Fig. 2. QCA-based definition of the atherosclerotic lesion. The vessel cross-section presenting the minimum lumen area (MLA) was identified as the section located in correspondence of the absolute minimum of the (measured) lumen area curve along the RCA centerline. The proximal and distal cross-sections delimiting the lesion segment were identified by the intersections between the lumen area curve along the RCA centerline and its regression line located immediately upstream and downstream of the MLA section, respectively. A 3D visualization of the lesion segment identified according to the QCA-based approach is here reported for an explanatory RCA model.

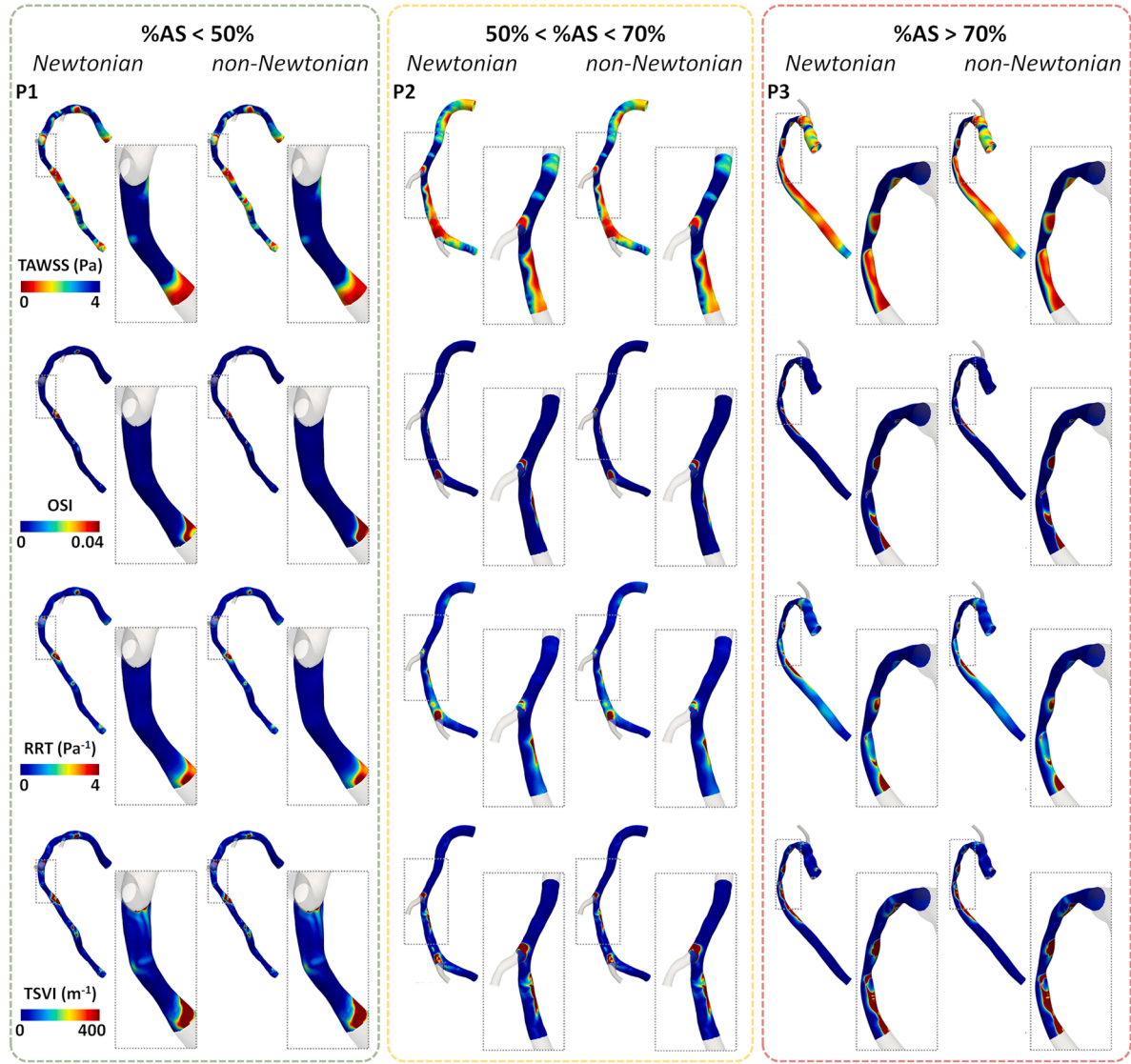


Fig. 3. Luminal surface area distributions of Newtonian vs. non-Newtonian near-wall hemodynamic quantities (Part 1). Distributions at the luminal surface of TAWSS, OSI, RRT, and TSVI are reported for one representative coronary model for each %AS class. A zoom view at the lesion level is also reported.

3.1. Near-wall hemodynamics

The distributions at the luminal surface of the WSS-based quantities obtained from N and non-N simulations are presented in Figs. 3 and 4 for one explanatory RCA case per %AS class, namely vessels P1 (class C1), P2 (class C2) and P3 (class C3). In detail, for each class the RCA model with %AS value closest to the median value of the class was selected. Overall and independent of the %AS, the N and non-N simulations present very similar luminal surface distributions of the WSS-based quantities TAWSS, OSI, RRT, TSVI (Fig. 3), transWSS, TAWSS_{ax}, and TAWSS_{sc} (Fig. 4). This observation can be extended to all the 144 RCAs under investigation.

The qualitative findings in Figs. 3 and 4 are confirmed by the quantitative analysis reported in Figs. 5 and 6, where distributions of the values of the WSS-based quantities are reported for 9 coronary vessels, selected according to the following scheme: the distributions obtained with N and non-N simulations on vessels P1, P2 and P3, representative of the median vessel of %AS classes C1, C2 and C3, respectively, are presented with cases representing the 25th percentile (vessel P4, class C1; vessel P6, class C2, and vessel P8, class C3) and the 75th percentile (vessel P5, class C1; vessel P7, class C2, and vessel P9, class C3) of each %AS class. The results in Figs. 5 and 6 confirm that the distribution of all the WSS-based quantities in the N and non-N case are very similar in shape (all right-skewed distributions with the same number of peaks). The expected overall increase of TAWSS and TSVI values with %AS emerged from the analysis (Fig. 5), while an overall modest WSS multidirectionality was expressed by OSI (mostly lower than 0.005, Fig. 5) and transWSS (lower than 1 Pa, Fig. 6).

The impact of the rheological properties set for simulating coronary

blood flows was evaluated comparing the median values of the luminal distributions of the WSS-based quantities at lesion level in terms of Bland-Altman plots, where data from non-N simulations were adopted as reference. Summarizing the results of the Bland-Altman plots (Figs. 7 and 8), it emerged that independent of the %AS class and for all the WSS-based quantities, the differences within 2 standard deviations from the mean difference interval were remarkably small, compared to the range of mean values (horizontal axis). In terms of bias, Figs. 7 and 8 highlighted the absence of a considerable mean bias for OSI, RRT, TSVI, transWSS, and TAWSS_{sc}, while a negative bias around 0.1 Pa emerged for TAWSS and TAWSS_{ax}. This indicated that using a Newtonian model for blood rheology might underestimate WSS magnitude, particularly where TAWSS and TAWSS_{ax} values are lower.

The values of Pearson's product moment correlation (Figs. 7 and 8) highlighted the existence of: (1) a positive linear trend for OSI ($r=0.57$, $p<0.001$, class C1), RRT ($r\geq 0.92$, $p<0.001$, all %AS classes), TSVI ($r\geq 0.72$, $p<0.001$, class C1 and C3), indicating that the error (i.e., the difference between N and non-N data) might increase with the increasing values of such WSS-based quantities and in particular in patients with low or high %AS; (2) a negative (always weaker than positive trends per point before) linear trend for TAWSS ($r=-0.37$, $p=0.01$, class C1), OSI ($r=-0.45$, $p<0.001$, class C2), transWSS ($r=-0.43$, $p<0.001$, class C2), TAWSS_{ax} ($r=-0.50$ and -0.24 , $p<0.001$ and $p=0.03$, for class C1 and C2, respectively), and TAWSS_{sc} ($r=-0.46$, $p<0.001$, class C2), indicating that the error might decrease with the increasing values of such WSS-based quantities and in particular in patients with low or moderate %AS. Overall, data from the Bland-Altman plots should be interpreted reminding that OSI values range between 0 and 0.5 while the other WSS-based quantities here considered are not bounded superiorly,

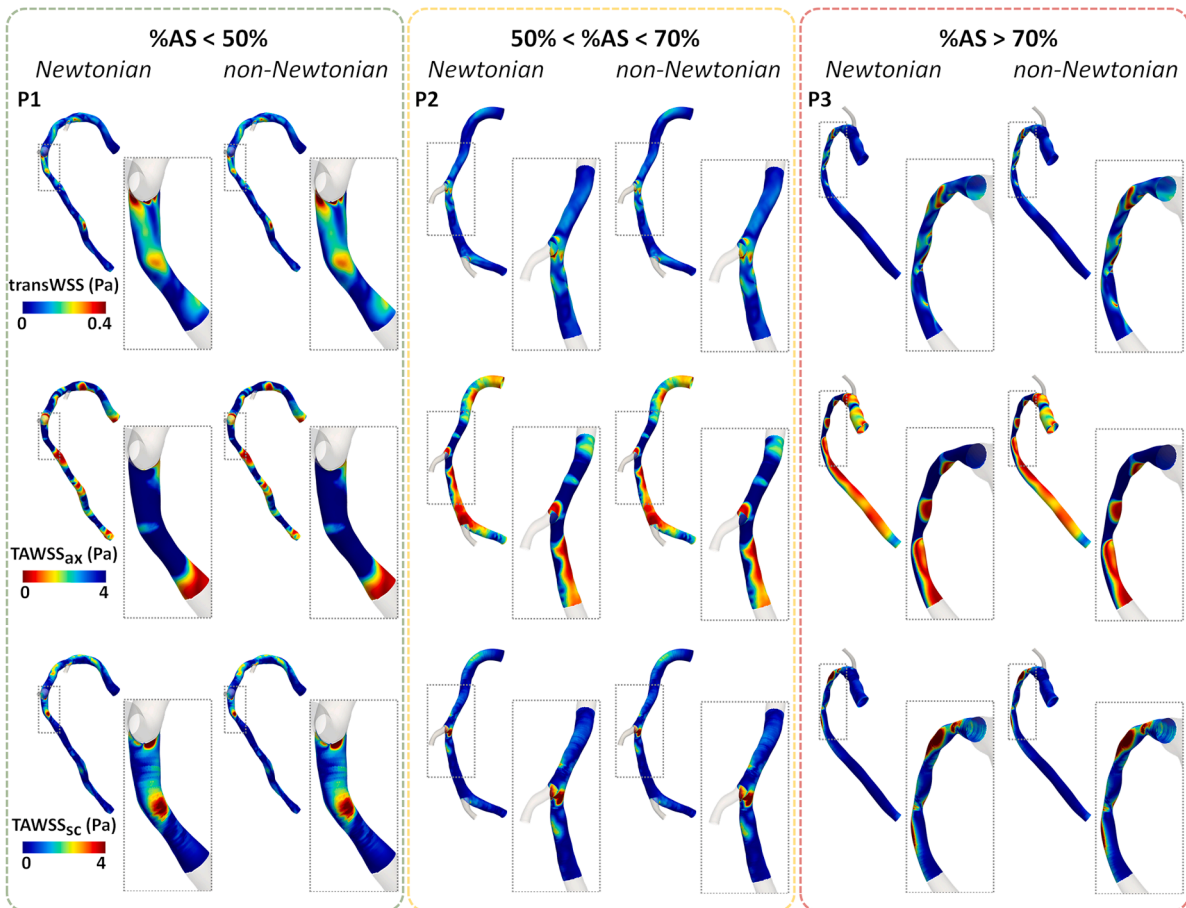


Figure 4. Luminal surface area distributions of Newtonian vs. non-Newtonian near-wall hemodynamic quantities (Part 2). Distributions at the luminal surface of transWSS, TAWSS_{ax}, and TAWSS_{sc} are reported for one representative coronary model for each %AS class. A zoom view at the lesion level is also reported.

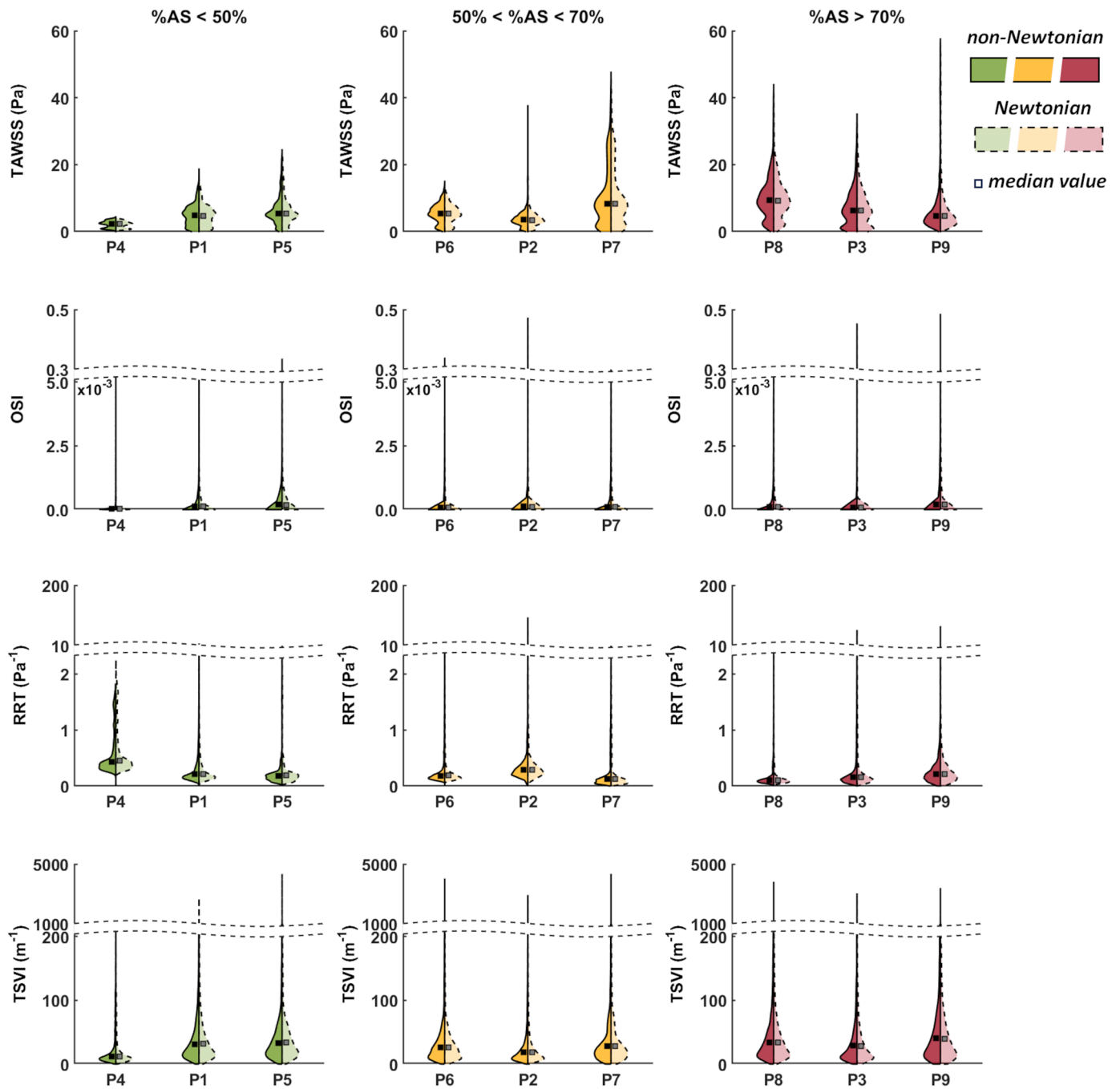


Fig. 5. Comparison of the luminal distributions of near-wall hemodynamic quantities from Newtonian and non-Newtonian CFD simulations (Part 1). Probability density functions and median values are presented using half violin plots visualization. To better appreciate differences in the distributions, a scale break was applied on the y axis for some quantities (OSI, RRT, and TSVI). The RCAs are grouped with respect to %AS: <50% (C1 - green colored); between 50% and 70% (C2 - yellow colored); >70% (C3 - red colored). Three representative cases per each %AS class are reported: cases P1, P2 and P3, representative of the median vessel of %AS classes C1, C2 and C3, respectively, are presented with cases representing the 25th percentile (vessel P4, class C1; vessel P6, class C2, and vessel P8, class C3) and the 75th percentile (vessel P5, class C1; vessel P7, class C2, and vessel P9, class C3) of each %AS class.

by construction.

The comparison between paired WSS-based quantities from N and non-N simulations was extended to all the luminal nodal values of the RCA models at the lesion level, where the existence of linear relationships was evaluated in terms of Pearson's correlation coefficient. Overall and independent of %AS, a very strong linear relationship emerged between N and non-N based paired near-wall quantities ($r > 0.94$, $p < 0.001$, for all the WSS-based quantities except for RRT, $0.70 \leq r \leq 0.80$, $p < 0.001$; Figures S2 and S3 in the Supplementary Material).

3.2. Intravascular hemodynamics

Helical blood flow patterns as obtained from N and non-N simulations in the three representative RCA models P1, P2 and P3, are visualized in terms of cycle-average LNH isosurfaces in Fig. 9. By visual inspection, the expected [13,14] two distinguishable counter-rotating helical flow patterns characterizing the simulated RCA hemodynamics clearly appear as not being dependent on %AS class, with their structure being not affected by the rheology-modelling strategy (Fig. 9).

The Bland-Altman plots were used to evaluate the impact of the

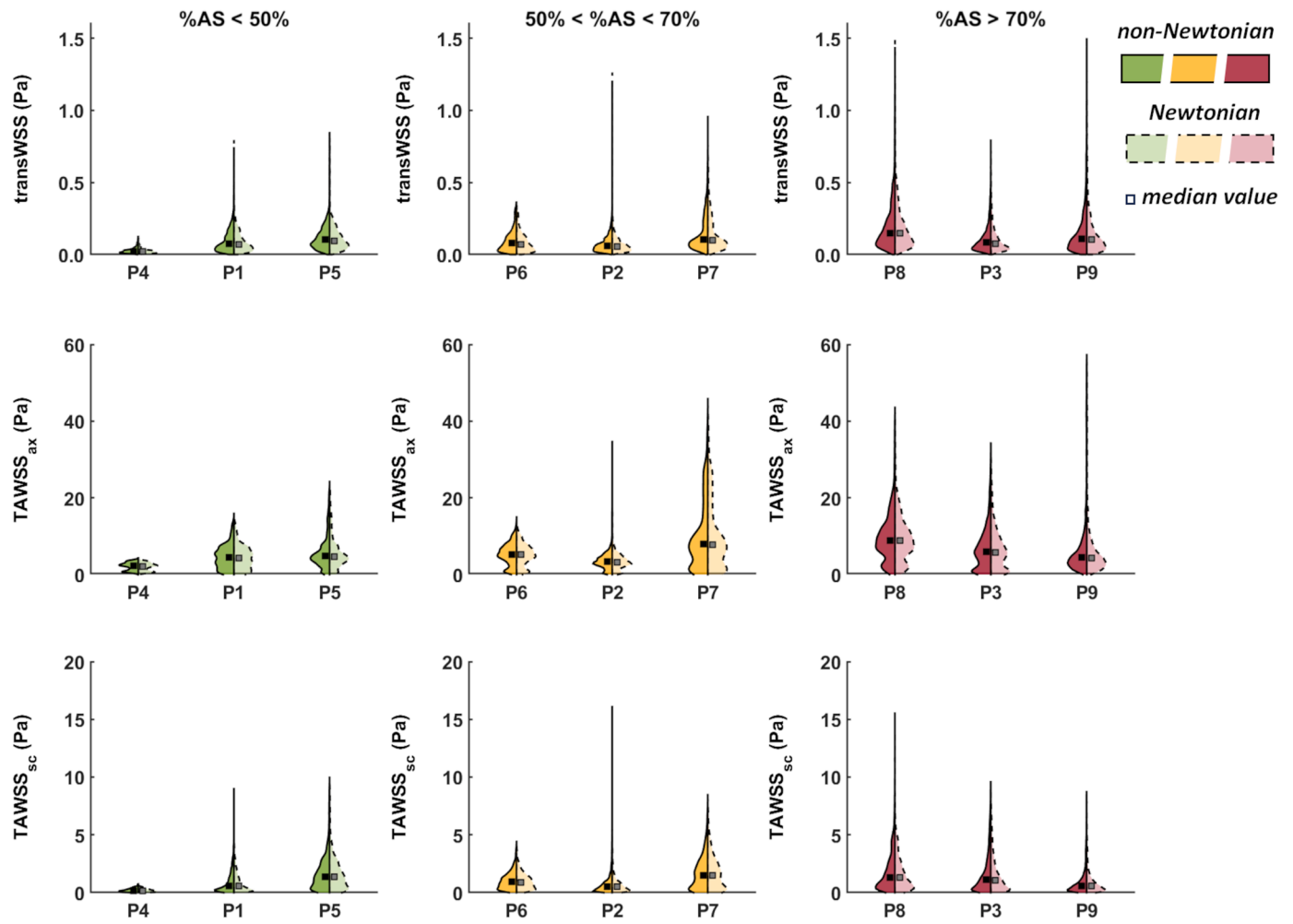


Fig. 6. Comparison of the luminal distributions of near-wall hemodynamic quantities from Newtonian and non-Newtonian CFD simulations (Part 2). Probability density functions and median values are presented using half violin plots visualization. The RCAs are grouped with respect to %AS: <50% (C1 - green colored); between 50% and 70% (C2 - yellow colored); >70% (C3 - red colored). Three representative cases per each %AS class are reported: cases P1, P2 and P3, representative of the median vessel of %AS classes C1, C2 and C3, respectively, are presented with cases representing the 25th percentile (vessel P4, class C1; vessel P6, class C2, and vessel P8, class C3) and the 75th percentile (vessel P5, class C1; vessel P7, class C2, and vessel P9, class C3) of each %AS class.

differently simulated rheological properties on helicity-based quantities at the lesion level (Fig. 10). As for WSS-based quantities, data from non-N simulations were adopted as reference. Overall, it emerged that independent of the %AS and for all the helicity-based quantities, the provided differences within 2 standard deviations from the mean difference interval were remarkably small, compared to the range of mean values (horizontal axis, Fig. 10). Moreover, the absence of a consistent bias clearly emerged for h_1 , h_2 , h_3 and h_4 . The values of Pearson's product moment correlation highlighted (Fig. 10) a positive linear trend in Bland-Altman plots of all the helicity-based quantities, which was stronger for cycle-average helicity h_1 ($r=0.89$ and 0.55 , $p<0.001$, for class C1 and C2, respectively) and helicity intensity h_2 ($r\geq 0.65$, $p<0.01$, all %AS classes), and weaker for quantities related to helical structures topology h_3 ($r\geq 0.46$, $p<0.01$, class C1 and C2) and h_4 ($r=0.28$, $p=0.01$, class C2). This indicates that the error (in terms of difference between N and non-N simulations) tends to increase with the increasing magnitude of h_1 quantities, in particular in RCA models with low-to-moderate %AS. Overall, data from the Bland-Altman plots should be interpreted reminding that h_3 values range between -1 and 1, and h_4 values range between 0 and 1, while h_1 and h_2 are not bounded superiorly, by construction.

The analysis was completed testing for the existence of linear relationships between paired intravascular quantities from N and non-N

simulations at the lesion level of the RCA models. Overall and independent of %AS, a very strong linear relationship emerged between N- and non-N- based paired intravascular h_1 quantities ($r>0.99$, $p<0.001$; Figure S4, Supplementary Material).

3.3. Analysis at the luminal surface area extension level

Fig. 11 reports the boxplots of similarity index values assessing the co-localization between N- and non-N-based disturbed SAs performed at vessel level. No remarkable differences emerged in the extension of disturbed SAs as obtained from N and non-N simulations. Median [interquartile range] SI values close to one resulted for all the investigated near-wall hemodynamic quantities ($SI_{LSA}=0.94$ [0.91, 0.98]; $SI_{HSA}=0.98$ [0.97, 0.99]; $SI_{OSA}=0.96$ [0.94, 0.97]; $SI_{RSA}=0.94$ [0.91, 0.98]; $SI_{TSVA}=0.95$ [0.93, 0.98]; $SI_{transSA}=0.91$ [0.88, 0.94]; $SI_{LaxSA}=0.94$ [0.91, 0.98]; $SI_{HaxSA}=0.98$ [0.96, 0.99]; $SI_{HscSA}=0.98$ [0.97, 0.99]). The overall median value of SI equal to 0.95 clearly highlighted the strong similarity of N- and non-N-based paired SAs.

4. Discussion

In the context of coronary artery disease, endothelial shear stress has emerged as a biomechanical marker of atherosclerosis, by virtue of its

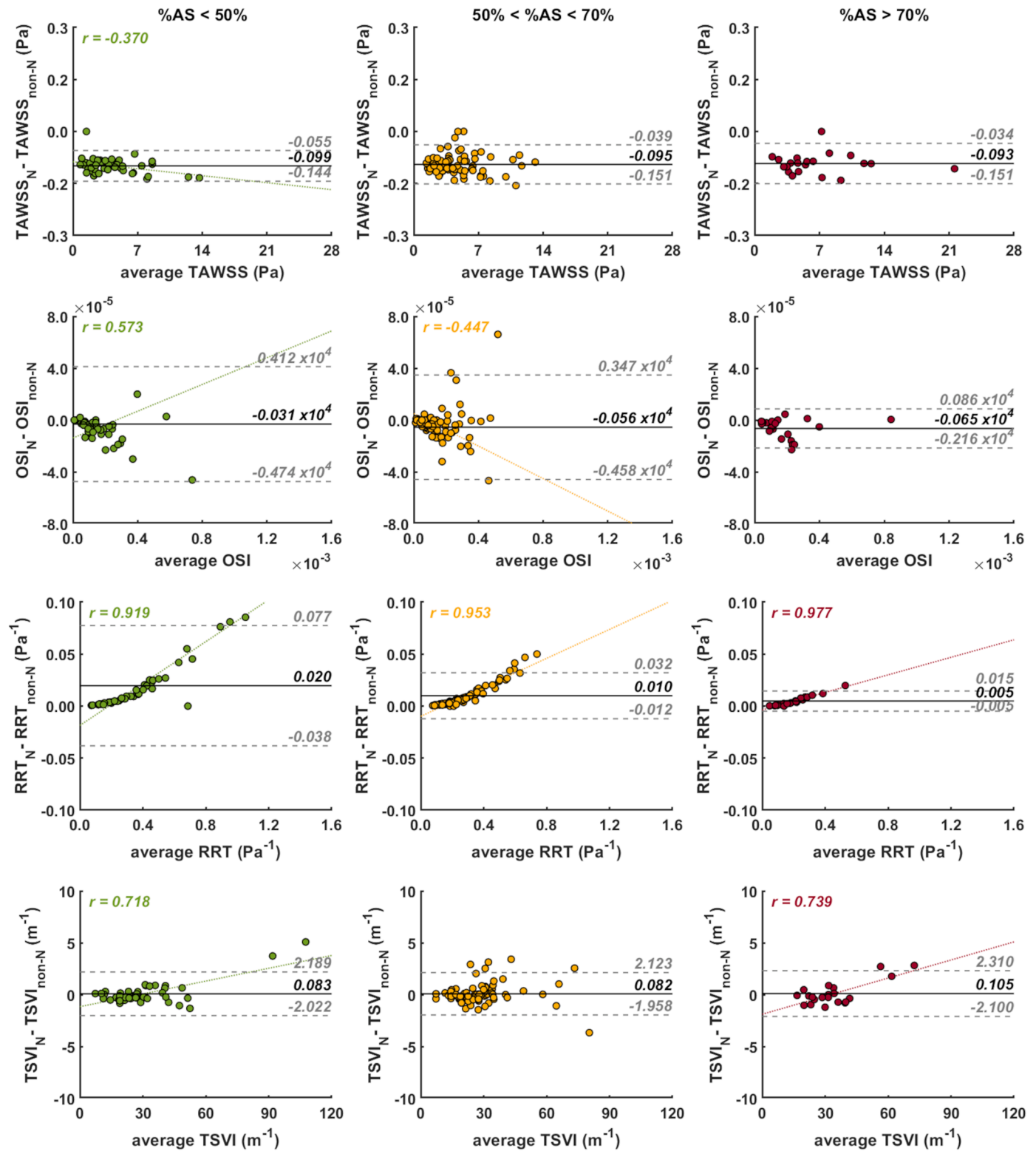


Fig. 7. Bland-Altman plots to evaluate the equivalence of the near-wall hemodynamic quantities from paired Newtonian and non-Newtonian CFD simulations (Part 1). For each near-wall hemodynamic quantity, the Bland-Altman plot of N vs. non-N median values at the lesion level is reported. Bias and 95% limits of agreements are also displayed (black line and grey dashed lines, respectively). Bland-Altman plots are presented for each %AS: <50% (green colored); between 50% and 70% (yellow colored); >70% (red colored). For significant (p<0.05) linear trend of the error, Pearson correlation coefficient (r) and regression line are displayed.

involvement in the onset and progression of adverse biological events [3,11,40,41]. Additionally, coronary helical flow has emerged as instrumental in suppressing flow disturbances [14], thus playing an atheroprotective role [13].

The inability of current medical technologies in accurately measuring *in vivo* those biomechanical markers in coronary arteries [42, 43] can be overcome incorporating personalized computational hemodynamics simulations into the clinical practice, with the final aim of

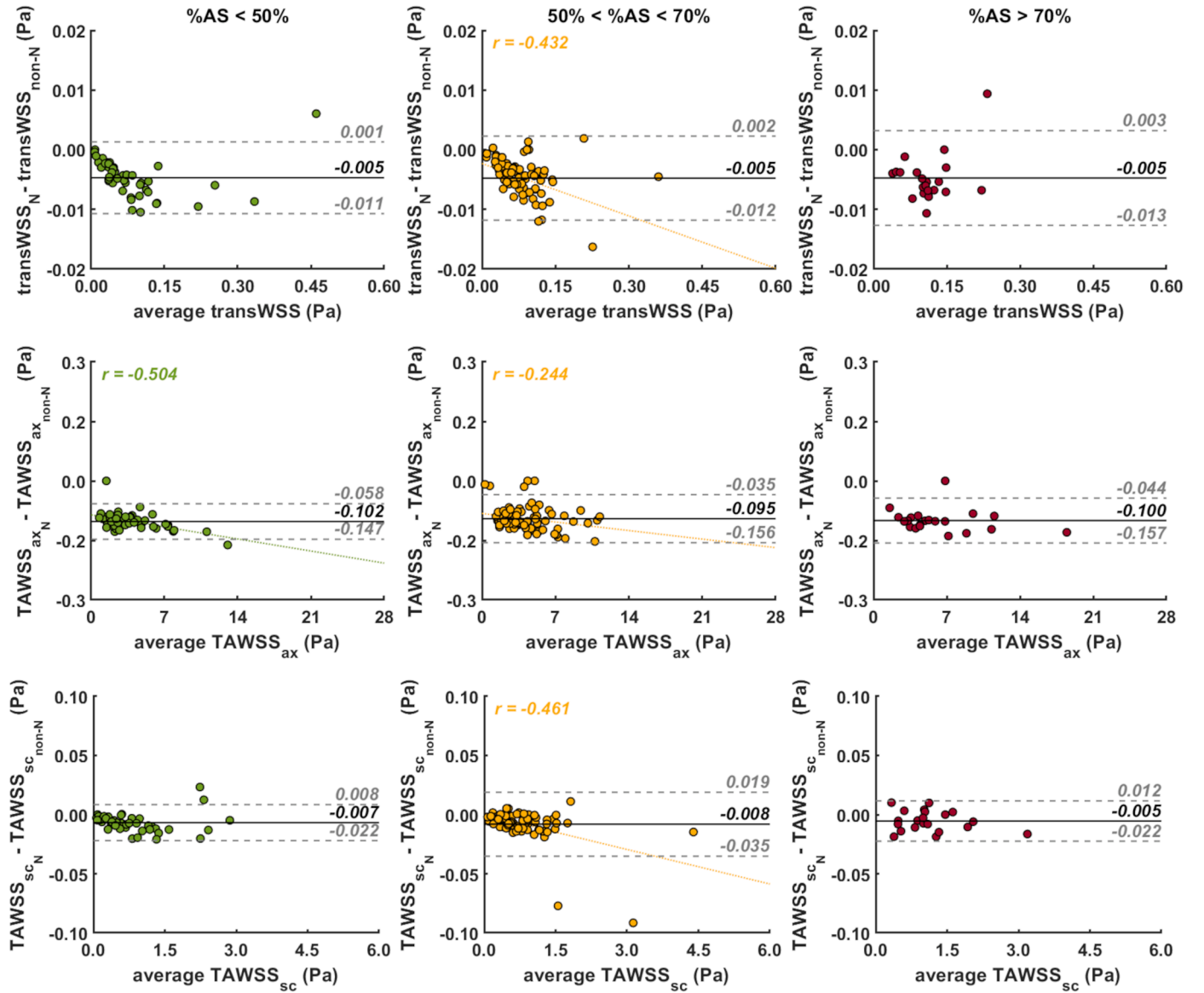


Fig. 8. Bland-Altman plots to evaluate the equivalence of the near-wall hemodynamic quantities from paired Newtonian and non-Newtonian CFD simulations (Part 2). For each near-wall hemodynamic quantity, the Bland-Altman plot of N vs. non-N median values at the lesion level is reported. Bias and 95% limits of agreements are also displayed (black line and grey dashed lines, respectively). Bland-Altman plots are presented for each %AS: <50% (green colored); between 50% and 70% (yellow colored); >70% (red colored). For significant ($p < 0.05$) linear trend of the error, Pearson correlation coefficient (r) and regression line are displayed.

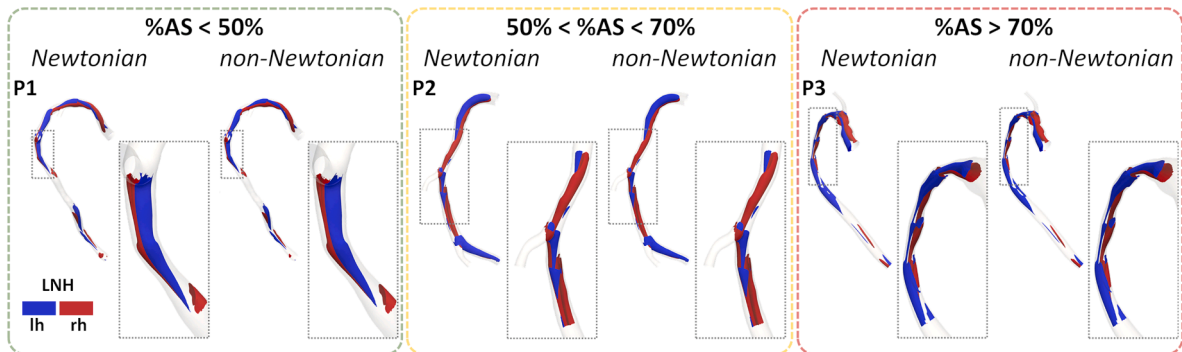


Fig. 9. Visualization of helical flow profile as obtained from Newtonian and non-Newtonian CFD simulations. Cardiac cycle-average LNH isosurfaces are reported for one representative coronary model for each %AS class. Blue and red colors identify the left- and right-handed rotational direction of helical fluid structures, respectively. A zoom view at the lesion level is also reported.

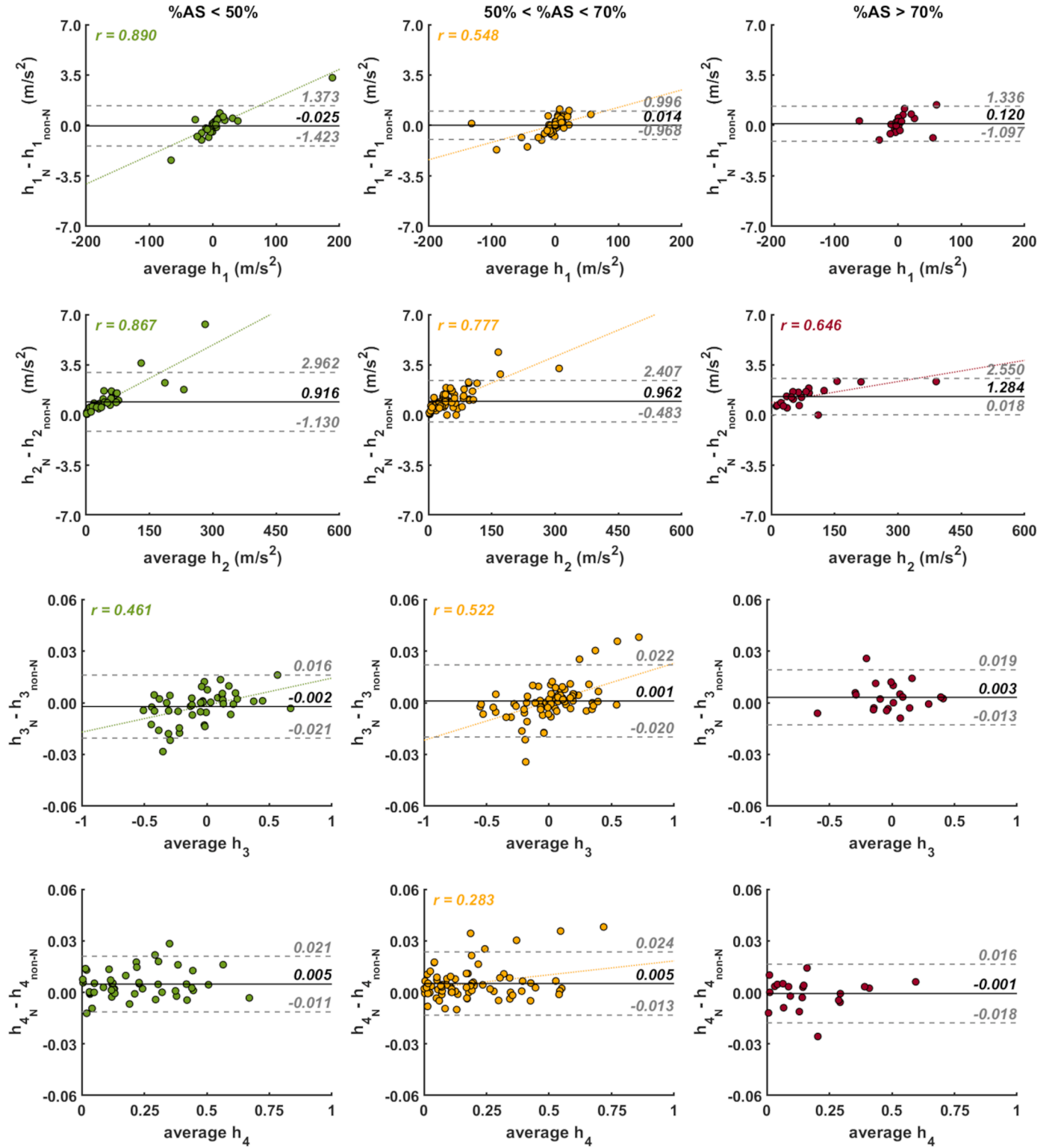


Fig. 10. Bland-Altman plots to evaluate the equivalence of the intravascular helical flow patterns from paired Newtonian and non-Newtonian CFD simulations. For each helicity-based quantity, the Bland-Altman plot of N vs. non-N values at the lesion level is reported. Bias and 95% limits of agreements are also displayed (black line and grey dashed lines, respectively). Bland-Altman plots are presented for each %AS: $<50\%$ (green colored); between 50% and 70% (yellow colored); $>70\%$ (red colored). For significant ($p < 0.05$) linear trend of the error, Pearson correlation coefficient (r) and regression line are displayed.

improving/enabling prognostics as well as preemptive treatment strategies [2]. To pursue this goal and to promote computational hemodynamics as a medical technology, the budget of uncertainty associated with modeling must be mandatorily delineated [16] and an overall standardization strategy must be identified.

Aiming at contributing to this achievement, in this study a comparative analysis between two different strategies which are largely adopted to model the rheological properties of blood in coronary hemodynamics simulations was performed. In detail, the impact of assuming Newtonian vs. shear-thinning non-Newtonian rheological

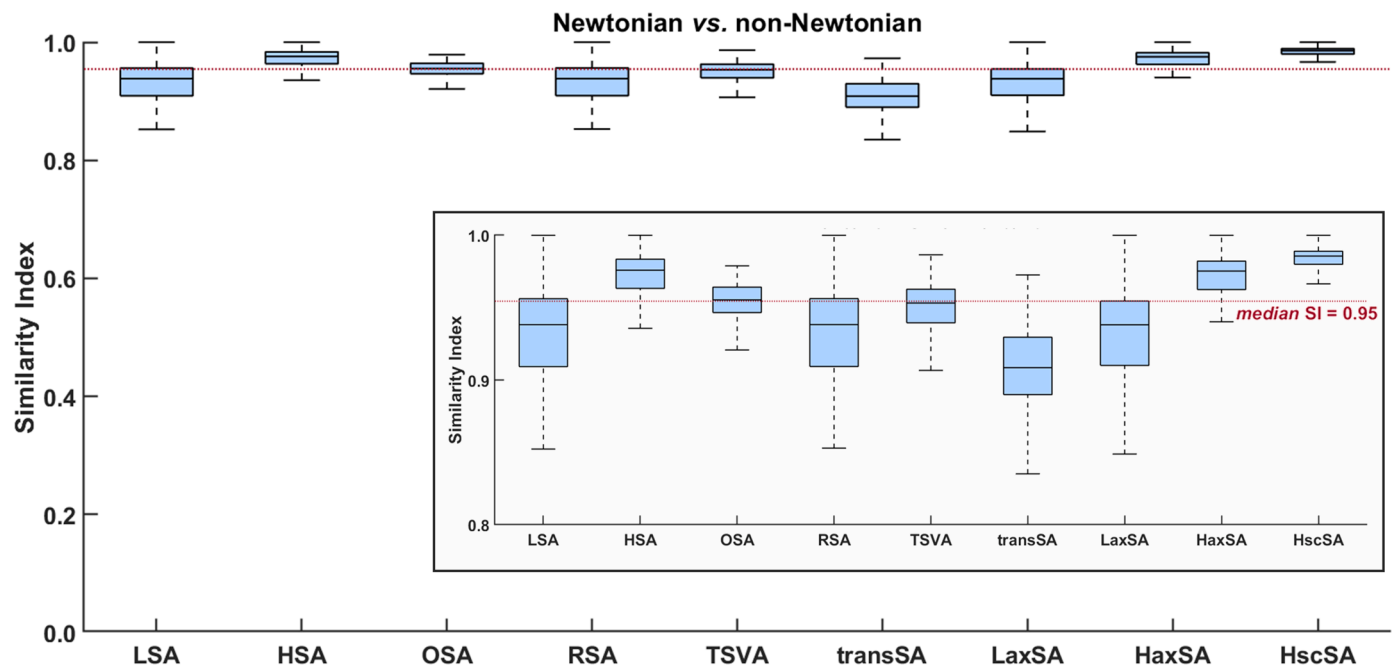


Fig. 11. Co-localization analysis of WSS-based luminal SAs exposed to flow disturbances from paired Newtonian and non-Newtonian CFD simulations. Boxplot visualization of Similarity Index (SI) values is adopted, displaying median value, interquartile range, and distribution bounds. LSA: low shear area; HSA: high shear area; oscillatory shear area: OSA; residence shear area: RSA; topological shear variation area: TSVA, transverse shear area: transSA; low axial shear area: LaxSA; high axial shear area: HaxSA; high secondary shear area: HscSA.

properties for blood was evaluated on a large dataset of patient-specific angiography-based *in silico* models of right coronary arteries in terms of near-wall and intravascular hemodynamic quantities which have been linked to biological adverse events.

The main findings of the study suggest that in coronary hemodynamics simulations, assumptions done on blood rheology (Figs. 3–11): (i) have negligible impact on WSS profiles in terms of both magnitude and multidirectionality (quantified in terms of OSI, transWSS, and TAWSS_{co}); (ii) do not affect the variability in WSS contraction/expansion action at the endothelium during cardiac cycle, quantified in terms of TSVI; (iii) have scarce impact on helical flow topology and intensity; (iv) scarcely affect the extent of the luminal SAs exposed to disturbed hemodynamics.

The present analysis was performed on a dataset of 144 RCA geometries, and it represents the largest study to date on the impact of blood rheology on coronary hemodynamic quantities of biological/clinical interest. This study suggests that the adoption of a shear-thinning non-Newtonian model could be unnecessary, independent of the degree of stenosis (within the explored range) of the coronary vessel. This result is in contrast with previously reported findings on the significant underestimation of WSS offered by the adoption of a Newtonian model, when compared to a non-Newtonian one [21–23,44,45]. In this regard, Johnston and coworkers [22] suggested that the implementation of a non-Newtonian model is needed to study the coronary flow with greater accuracy and detail, while Thondapu and colleagues [21] claimed that non-Newtonian behavior of blood is operational, yielding marked differences in hemodynamics indices such as WSS and WSS gradient. Additionally, Liu and Tang [44] claimed out that the blood rheological properties have considerable effect on WSS magnitude, especially where disturbed flow is observed, while Apostolidis and colleagues [45] reported significant differences (up to 50%) between the simulation output of Newtonian and non-Newtonian models. Very recently, Kandangwa et al. [23] suggested that simulating artery motion and non-N blood rheological behaviour in a computational model of the RCA hemodynamics might have not negligible impact on OSI and transWSS and a limited effect on TAWSS. All these reference studies as

well as the body of literature available on the argument suffer from the very limited number of cases investigated (e.g., 4 patient-specific geometries were analysed by Johnston et al. [22], 16 by Thondapu et al. [21], 1 by Liu and Tang [44]; 1 idealized geometry was analysed by Apostolidis et al. [45]). Moreover, such studies emphasized instantaneous differences of paired N vs. non-N simulated WSS data [21,22,44] rather than cycle-average WSS-based quantities, although the latter are the ones emerged to be linked to CAD manifestations. Additionally, the reported global non-Newtonian importance factor [46], weighting the difference of N vs. non-N dynamic viscosity, resulted in a very low time-average value (<0.3) [22], suggesting a poor-to-moderate impact of the shear-thinning phenomenon on cardiac-cycle average WSS profiles.

The emerged discrepancies between our findings and previous studies may be attributed in part to the analysis of idealized [45] coronary artery models [21,22,44] or, more probably, to the low cardinality of the analysed datasets, which might not be sufficiently representative of the variability of a population [21–23,44].

As a remarkable finding of the study, we highlight here that the obtained equivalence of paired N vs. non-N simulations in terms of WSS-based quantities emerges in all the three %AS interval values analysed. Finally, the emerged marked overlap (>80%) of paired N and non-N luminal SAs exposed to disturbed hemodynamics (Fig. 11) unambiguously testify the capability of the Newtonian rheological assumptions to identify colocalized luminal regions more prone to CAD onset/development, with a median co-localization of 95%. This might have clinical translational implications: since clinicians require absolute threshold values for CAD risk quantification and stratification [2,3,11], the reported findings suggest that the selected model for coronary blood flow rheology has a minor importance. This is especially true if modelling assumptions, computational settings and the definition of threshold values for the hemodynamic quantities of clinical interest undergo a standardization that would make computational hemodynamics simulations reproducible, i.e. capable to provide comparable results when applied to similar populations.

4.1. Limitations

Some limitations could weaken the findings of this study. The uncertainty and the level of idealization inherent in the computational hemodynamic modelling might have influenced the considered near-wall and intravascular hemodynamic quantities. In particular, the rigid walls assumption and the absence of the cardiac-induced motion of coronary arteries could have affected the WSS estimation. However, the impact of such assumption on the WSS distribution has been demonstrated to be minor, especially when considering time-averaged and/or integral WSS quantities [47]. In this regard and for the sake of completeness, it must be mentioned here a very recent single-case study suggesting that including both artery motion and non-N blood rheology in CFD simulations of the RCA hemodynamics might have consequences on secondary flow patterns that not linearly pile up and might amplify the impact of blood rheological properties on quantities measuring WSS multidirectionality [23].

Additionally, the lack of personalized instantaneous flow measurements and the assumptions made to manage the inflow boundary conditions could have affected WSS and velocity estimation. However, the use of generic Doppler velocity curves scaled to fit patient-specific inlet cross-section diameter was previously validated [32], and its impact on coronary hemodynamic quantities is expected to be even minor when using frame count data to determine the patient-specific cycle-average flow rate [31].

The limitations discussed above are expected to impact equally on N and non-N CFD simulations, with no effect on the reported findings.

Another possible limitation of the study concerns the selection of a single value of Newtonian dynamic viscosity for all the patients, corresponding to a hematocrit value representative of the physiological hematocrit range variation [29]. In the future, the influence of patient-specific hematocrit values on both shear-thinning and Newtonian rheological model should be investigated more in depth.

Finally, the study was focused only on patient-specific right coronary arteries, not involving left anterior descending (LAD) nor left circumflex (LCX) coronary vessels. However, a recent study [48] revealed a marked similarity of near-wall and intravascular hemodynamic quantities among the three main coronary arteries (i.e., RCA, LAD, and LCX), which suggests extending the present findings to all epicardial coronary segments. On the contrary, it is not possible to generalize the emerged evidence to smaller coronary segments, in which the shear-thinning and viscoelastic behaviors [49] of blood might gain relevance. This stimulates future investigation on the impact of N vs. non-N rheological assumption on the hemodynamics of smaller arteries and on the effect of the elastic response of blood viscoelasticity in coronary hemodynamics [49].

4.2. Conclusions

In this study the impact of assumptions on blood rheology in personalized computer simulations of coronary hemodynamics is evaluated on the largest dataset to date (144 right coronary arteries). The findings of the study clearly highlight that the assumptions on blood rheology have negligible impact on both WSS and helical flow profiles associated with coronary artery disease, thus definitively answering to the still *vexata quaestio* “Newtonian or shear-thinning non-Newtonian rheology in coronary hemodynamics simulations?”. The simpler and more computationally convenient assumption of Newtonian rheology for blood is acceptable when modelling coronary hemodynamics. Finally, the findings of the study are a further indication that standardization of *in silico* strategies is a primary effort to be pursued to gain credibility and encourage translation to clinics of computational hemodynamics.

Funding

This work has been supported by the Italian Ministry of Education, University and Research (FISR2019_03221, CECOMES).

Declaration of Competing Interest

AC reports having consultancy agreements with Medyria, HiD-Imaging and Nanoflex Robotics.

Supplementary materials

Supplementary material associated with this article can be found, in the online version, at [doi:10.1016/j.cmpb.2023.107823](https://doi.org/10.1016/j.cmpb.2023.107823).

References

- [1] U. Ralapanawa, R. Sivakanesan, Epidemiology and the Magnitude of Coronary Artery Disease and Acute Coronary Syndrome: A Narrative Review, *J Epidemiol Glob Health* 11 (2021) 169–177, <https://doi.org/10.2991/jegh.k.201217.001>.
- [2] A. Candreva, G. De Nisco, M. Lodi Rizzini, F. D'Ascenzo, G.M. De Ferrari, D. Gallo, U. Morbiducci, C. Chiastra, Current and Future Applications of Computational Fluid Dynamics in Coronary Artery Disease, *RCM* 23 (2022) 377, <https://doi.org/10.31083/j.rcm2311377>.
- [3] A. Candreva, M. Pagnoni, M.L. Rizzini, T. Mizukami, E. Gallinoro, V. Mazzi, D. Gallo, D. Meier, T. Shinke, J.-P. Aben, S. Nagumo, J. Sonck, D. Munhoz, S. Fournier, E. Barbato, W. Heggermont, S. Cook, C. Chiastra, U. Morbiducci, B. De Bruyne, O. Muller, C. Collet, Risk of myocardial infarction based on endothelial shear stress analysis using coronary angiography, *Atherosclerosis* 342 (2022) 28–35, <https://doi.org/10.1016/j.atherosclerosis.2021.11.010>.
- [4] A.J. Brown, Z. Teng, P.C. Evans, J.H. Gillard, H. Samady, M.R. Bennett, Role of biomechanical forces in the natural history of coronary atherosclerosis, *Nat Rev Cardiol* 13 (2016) 210–220, <https://doi.org/10.1038/nrcardio.2015.203>.
- [5] F. Gijzen, Y. Katagiri, P. Barlis, C. Bourantas, C. Collet, U. Coskun, J. Daemen, J. Dijkstra, E. Edelman, P. Evans, K. van der Heiden, R. Hose, B.-K. Koo, R. Krams, A. Marsden, F. Migliavacca, Y. Onuma, A. Ooi, E. Poon, H. Samady, P. Stone, K. Takahashi, D. Tang, V. Thondapu, E. Tenekcioglu, L. Timmins, R. Torii, J. Wentzel, P. Serruys, Expert recommendations on the assessment of wall shear stress in human coronary arteries: existing methodologies, technical considerations, and clinical applications, *Eur Heart J* 40 (2019) 3421–3433, <https://doi.org/10.1093/eurheartj/ehz551>.
- [6] R. Pandey, M. Kumar, J. Majdoubi, M. Rahimi-Gorji, V.K. Srivastav, A review study on blood in human coronary artery: Numerical approach, *Comput Methods Programs Biomed* 187 (2020), 105243, <https://doi.org/10.1016/j.cmpb.2019.105243>.
- [7] U. Morbiducci, A.M. Kok, B.R. Kwak, P.H. Stone, D.A. Steinman, J.J. Wentzel, Atherosclerosis at arterial bifurcations: Evidence for the role of haemodynamics and geometry, *Thromb Haemost* 115 (2016) 484–492, <https://doi.org/10.1160/TH15-07-0597>.
- [8] Y.S. Chatzizisis, A.U. Coskun, M. Jonas, E.R. Edelman, C.L. Feldman, P.H. Stone, Role of endothelial shear stress in the natural history of coronary atherosclerosis and vascular remodeling: molecular, cellular, and vascular behavior, *J Am Coll Cardiol* 49 (2007) 2379–2393, <https://doi.org/10.1016/j.jacc.2007.02.059>.
- [9] H. Samady, P. Eshtehardi, M.C. McDaniel, J. Suo, S.S. Dhawan, C. Maynard, L. H. Timmins, A.A. Quyyumi, D.P. Giddens, Coronary artery wall shear stress is associated with progression and transformation of atherosclerotic plaque and arterial remodeling in patients with coronary artery disease, *Circulation* 124 (2011) 779–788, <https://doi.org/10.1161/CIRCULATIONAHA.111.021824>.
- [10] J.J. Wentzel, Y.S. Chatzizisis, F.J.H. Gijzen, G.D. Giannoglou, C.L. Feldman, P. H. Stone, Endothelial shear stress in the evolution of coronary atherosclerotic plaque and vascular remodelling: current understanding and remaining questions, *Cardiovasc Res* 96 (2012) 234–243, <https://doi.org/10.1093/cvr/cvs217>.
- [11] A. Kumar, E.W. Thompson, A. Lefieux, D.S. Molony, E.L. Davis, N. Chand, S. Fournier, H.S. Lee, J. Suh, K. Sato, Y.-A. Ko, D. Molloy, K. Chandran, H. Hosseini, S. Gupta, A. Milkas, B. Gogas, H.-J. Chang, J.K. Min, W.F. Fearon, A. Venezianni, D. P. Giddens, S.B. King, B. De Bruyne, H. Samady, High Coronary Shear Stress in Patients With Coronary Artery Disease Predicts Myocardial Infarction, *J Am Coll Cardiol* 72 (2018) 1926–1935, <https://doi.org/10.1016/j.jacc.2018.07.075>.
- [12] V. Mazzi, G. De Nisco, A. Hoogendoorn, K. Calò, C. Chiastra, D. Gallo, D. A. Steinman, J.J. Wentzel, U. Morbiducci, Early Atherosclerotic Changes in Coronary Arteries are Associated with Endothelium Shear Stress Contraction/Expansion Variability, *Ann Biomed Eng* 49 (2021) 2606–2621, <https://doi.org/10.1007/s10439-021-02829-5>.
- [13] G. De Nisco, A. Hoogendoorn, C. Chiastra, D. Gallo, A.M. Kok, U. Morbiducci, J. J. Wentzel, The impact of helical flow on coronary atherosclerotic plaque development, *Atherosclerosis* 300 (2020) 39–46, <https://doi.org/10.1016/j.atherosclerosis.2020.01.027>.
- [14] G. De Nisco, A.M. Kok, C. Chiastra, D. Gallo, A. Hoogendoorn, F. Migliavacca, J. J. Wentzel, U. Morbiducci, The Atheroprotective Nature of Helical Flow in Coronary Arteries, *Ann Biomed Eng* 47 (2019) 425–438, <https://doi.org/10.1007/s10439-018-02169-x>.

- [15] P. Pathmanathan, R.A. Gray, V.J. Romero, T.M. Morrison, Applicability Analysis of Validation Evidence for Biomedical Computational Models, *J Verif Valid Uncertain Quantif* 2 (2017), <https://doi.org/10.1115/1.4037671>.
- [16] D.A. Steinman, F. Migliavacca, Editorial: Special Issue on Verification, Validation, and Uncertainty Quantification of Cardiovascular Models: Towards Effective VVUQ for Translating Cardiovascular Modelling to Clinical Utility, *Cardiovasc Eng Technol* 9 (2018) 539–543, <https://doi.org/10.1007/s13239-018-00393-z>.
- [17] G.B. Thurston, Rheological parameters for the viscosity viscoelasticity and thixotropy of blood, *Biorheology* 16 (1979) 149–162, <https://doi.org/10.3233/BIR-1979-16303>.
- [18] L. Campo-Deaño, R.P.A. Dullens, D.G.A.L. Aarts, F.T. Pinho, M.S.N. Oliveira, Viscoelasticity of blood and viscoelastic blood analogues for use in polydimethylsiloxane in vitro models of the circulatory system, *Biomicrofluidics* 7 (2013), 034102, <https://doi.org/10.1063/1.4804649>.
- [19] J.M. Sherwood, E. Kaliviotis, J. Dusing, S. Balabani, Hematocrit, viscosity and velocity distributions of aggregating and non-aggregating blood in a bifurcating microchannel, *Biomech Model Mechanobiol* 13 (2014) 259–273, <https://doi.org/10.1007/s10237-012-0449-9>.
- [20] S. Chien, S. Usami, R.J. Dellenback, M.I. Gregersen, Shear-dependent deformation of erythrocytes in rheology of human blood, *American Journal of Physiology-Legacy Content* 219 (1970) 136–142, <https://doi.org/10.1152/ajplegacy.1970.219.1.136>.
- [21] V. Thondapu, D. Shishikura, J. Dijkstra, S.J. Zhu, E. Revalor, P.W. Serruys, W. J. van Gaal, E.K.W. Poon, A. Ooi, P. Barlis, Non-Newtonian Endothelial Shear Stress Simulation: Does It Matter? *Front Cardiovasc Med* 9 (2022) <https://doi.org/10.3389/fcvm.2022.835270>.
- [22] B.M. Johnston, P.R. Johnston, S. Corney, D. Kilpatrick, Non-Newtonian blood flow in human right coronary arteries: Transient simulations, *J Biomech* 39 (2006) 1116–1128, <https://doi.org/10.1016/j.jbiomech.2005.01.034>.
- [23] P. Kandangwa, R. Torii, P.D. Gatehouse, S.J. Sherwin, P.D. Weinberg, Influence of right coronary artery motion, flow pulsatility and non-Newtonian rheology on wall shear stress metrics, *Front Bioeng Biotechnol* 10 (2022). <https://www.frontiersin.org/articles/10.3389/fbioe.2022.962687>.
- [24] A. Arzani, Accounting for residence-time in blood rheology models: do we really need non-Newtonian blood flow modelling in large arteries? *J R Soc Interface* 15 (2018), 20180486 <https://doi.org/10.1098/rsif.2018.0486>.
- [25] A.A. Giannopoulos, Y.S. Chatzizisis, P. Maurovich-Horvat, A.P. Antoniadis, U. Hoffmann, M.L. Steigner, F.J. Rybicki, D. Mitsouras, Quantifying the effect of side branches in endothelial shear stress estimates, *Atherosclerosis* 251 (2016) 213–218, <https://doi.org/10.1016/j.atherosclerosis.2016.06.038>.
- [26] M. Vardhan, J. Gounley, S.J. Chen, A.M. Kahn, J.A. Leopold, A. Randles, The importance of side branches in modeling 3D hemodynamics from angiograms for patients with coronary artery disease, *Sci Rep* 9 (2019) 8854, <https://doi.org/10.1038/s41598-019-45342-5>.
- [27] Y. Li, J.L. Gutiérrez-Chico, N.R. Holm, W. Yang, L. Hebsgaard, E.H. Christiansen, M. Mæng, J.F. Lassen, F. Yan, J.H.C. Reiber, S. Tu, Impact of Side Branch Modeling on Computation of Endothelial Shear Stress in Coronary Artery Disease: Coronary Tree Reconstruction by Fusion of 3D Angiography and OCT, *J Am Coll Cardiol* 66 (2015) 125–135, <https://doi.org/10.1016/j.jacc.2015.05.008>.
- [28] M. Lodi Rizzini, D. Gallo, G. De Nisco, F. D'Ascenzo, C. Chiastra, P.P. Bocchino, F. Piroli, G.M. De Ferrari, U. Morbiducci, Does the inflow velocity profile influence physiologically relevant flow patterns in computational hemodynamic models of left anterior descending coronary artery? *Med Eng Phys* 82 (2020) 58–69, <https://doi.org/10.1016/j.medengphys.2020.07.001>.
- [29] U. Morbiducci, D. Gallo, D. Massai, R. Ponzini, M.A. Deriu, L. Antiga, A. Redaelli, F. M. Montecchi, On the importance of blood rheology for bulk flow in hemodynamic models of the carotid bifurcation, *J Biomech* 44 (2011) 2427–2438, <https://doi.org/10.1016/j.jbiomech.2011.06.028>.
- [30] V. Carvalho, D. Pinho, R.A. Lima, J.C. Teixeira, S. Teixeira, Blood Flow Modeling in Coronary Arteries: A Review, *Fluids* 6 (2021), <https://doi.org/10.3390/fluids6020053>.
- [31] M. Lodi Rizzini, A. Candrea, C. Chiastra, E. Gallinoro, K. Calò, F. D'Ascenzo, B. De Bruyne, T. Mizukami, C. Collet, D. Gallo, U. Morbiducci, Modelling coronary flows: impact of differently measured inflow boundary conditions on vessel-specific computational hemodynamic profiles, *Comput Methods Programs Biomed* 221 (2022), 106882, <https://doi.org/10.1016/j.cmpb.2022.106882>.
- [32] A.G. van der Giessen, H.C. Groen, P.-A. Doriot, P.J. de Feyter, A.F.W. van der Steen, F.N. van de Vosse, J.J. Wentzel, F.J.H. Gijzen, The influence of boundary conditions on wall shear stress distribution in patients specific coronary trees, *J Biomech* 44 (2011) 1089–1095, <https://doi.org/10.1016/j.jbiomech.2011.01.036>.
- [33] M. Mahmoudi, A. Farghadan, D.R. McConnell, A.J. Barker, J.J. Wentzel, M. J. Budoff, A. Arzani, The Story of Wall Shear Stress in Coronary Artery Atherosclerosis: Biochemical Transport and Mechanotransduction, *J Biomech Eng* 143 (2020), <https://doi.org/10.1115/1.4049026>.
- [34] D.N. Ku, D.P. Giddens, C.K. Zarins, S. Glagov, Pulsatile flow and atherosclerosis in the human carotid bifurcation. Positive correlation between plaque location and low oscillating shear stress, *Arteriosclerosis* 5 (1985) 293–302, <https://doi.org/10.1161/01.ATV.5.3.293>.
- [35] H.A. Himburg, D.M. Grzybowski, A.L. Hazel, J.A. LaMack, X.-M. Li, M. H. Friedman, Spatial comparison between wall shear stress measures and porcine arterial endothelial permeability, *Am J Physiol Heart Circ Physiol* 286 (2004) H1916–H1922, <https://doi.org/10.1152/ajpheart.00897.2003>.
- [36] V. Peiffer, S.J. Sherwin, P.D. Weinberg, Computation in the rabbit aorta of a new metric - the transverse wall shear stress - to quantify the multidirectional character of disturbed blood flow, *J Biomech* 46 (2013) 2651–2658, <https://doi.org/10.1016/j.jbiomech.2013.08.003>.
- [37] D. Gallo, D.A. Steinman, P.B. Bijari, U. Morbiducci, Helical flow in carotid bifurcation as surrogate marker of exposure to disturbed shear, *J Biomech* 45 (2012) 2398–2404, <https://doi.org/10.1016/j.jbiomech.2012.07.007>.
- [38] D.G. Altman, J.M. Bland, Measurement in Medicine: The Analysis of Method Comparison Studies, *Journal of the Royal Statistical Society. Series D (The Statistician)*. 32 (1983) 307–317, <https://doi.org/10.2307/2987937>.
- [39] D. Gallo, D.A. Steinman, U. Morbiducci, Insights into the co-localization of magnitude-based versus direction-based indicators of disturbed shear at the carotid bifurcation, *J Biomech* 49 (2016) 2413–2419, <https://doi.org/10.1016/j.jbiomech.2016.02.010>.
- [40] A. Kumar, O.Y. Hung, M. Piccinelli, P. Eshtehardi, M.T. Corban, D. Sternheim, B. Yang, A. Lefieux, D.S. Molony, E.W. Thompson, W. Zeng, Y. Bouchi, S. Gupta, H. Hosseini, M. Raad, Y.-A. Ko, C. Liu, M.C. McDaniel, B.D. Gogas, J.S. Douglas, A. A. Quyyumi, D.P. Giddens, A. Veneziani, H. Samady, Low Coronary Wall Shear Stress Is Associated With Severe Endothelial Dysfunction in Patients With Nonobstructive Coronary Artery Disease, *JACC Cardiovasc Interv* 11 (2018) 2072–2080, <https://doi.org/10.1016/j.jcin.2018.07.004>.
- [41] H.J. Carpenter, M.H. Ghayesh, A.C. Zander, P.J. Psaltis, On the nonlinear relationship between wall shear stress topology and multi-directionality in coronary atherosclerosis, *Comput Methods Programs Biomed* 231 (2023), 107418, <https://doi.org/10.1016/j.cmpb.2023.107418>.
- [42] M. Markl, S. Schnell, C. Wu, E. Bollache, K. Jarvis, A.J. Barker, J.D. Robinson, C. K. Rigsby, Advanced flow MRI: emerging techniques and applications, *Clin Radiol* 71 (2016) 779–795, <https://doi.org/10.1016/j.crad.2016.01.011>.
- [43] A. Frydrychowicz, A. Berger, A. Munoz Del Rio, M.F. Russe, J. Bock, A. Harloff, M. Markl, Interdependencies of aortic arch secondary flow patterns, geometry, and age analysed by 4-dimensional phase contrast magnetic resonance imaging at 3 Tesla, *Eur Radiol* 22 (2012) 1122–1130, <https://doi.org/10.1007/s00330-011-2353-6>.
- [44] B. Liu, D. Tang, Influence of non-Newtonian Properties of Blood on the Wall Shear Stress in Human Atherosclerotic Right Coronary Arteries, *Molecular & Cellular Biomechanics* 8 (2011) 73–90, <https://doi.org/10.3970/mcb.2011.008.073>.
- [45] A.J. Apostolidis, A.P. Moyer, A.N. Beris, Non-Newtonian effects in simulations of coronary arterial blood flow, *J Nonnewton Fluid Mech* 233 (2016) 155–165, <https://doi.org/10.1016/j.jnnfm.2016.03.008>.
- [46] P.D. Ballyk, D.A. Steinman, C.R. Ethier, Simulation of non-Newtonian blood flow in an end-to-side anastomosis, *Biorheology* 31 (1994) 565–586, <https://doi.org/10.3233/BIR-1994-31505>.
- [47] R. Torii, J. Keegan, N.B. Wood, A.W. Dowsey, A.D. Hughes, G.-Z. Yang, D. N. Firmin, S.A.M. Thom, X.Y. Xu, MR image-based geometric and hemodynamic investigation of the right coronary artery with dynamic vessel motion, *Ann Biomed Eng* 38 (2010) 2606–2620, <https://doi.org/10.1007/s10439-010-0008-4>.
- [48] G. De Nisco, C. Chiastra, E.M.J. Hartman, A. Hoogendoorn, J. Daemen, K. Calò, D. Gallo, U. Morbiducci, J.J. Wentzel, Comparison of Swine and Human Computational Hemodynamics Models for the Study of Coronary Atherosclerosis, *Front Bioeng Biotechnol* 9 (2021), <https://doi.org/10.3389/fbioe.2021.731924>.
- [49] S.I.S. Pinto, E. Romano, C.C. António, L.C. Sousa, C.F. Castro, The impact of non-linear viscoelastic property of blood in right coronary arteries hemodynamics — A numerical implementation, *Int J Non Linear Mech* 123 (2020), 103477, <https://doi.org/10.1016/j.jnonlinmec.2020.103477>.